Nanoscale

PAPER

View Article Online
View Journal

Cite this: DOI: 10.1039/d1nr01442k

Intrinsic helical twist and chirality in ultrathin tellurium nanowires†

Alejandra Londoño-Calderon, [a] Darrick J. Williams,[a] Matthew M. Schneider,[b] Benjamin H. Savitzky,[c] Colin Ophus,[c] Sijie Ma,[d] Hanyu Zhu[d] and Michael T. Pettes *[a]

Robust atomic-to-meso-scale chirality is now observed in the one-dimensional form of tellurium. This enables a large and counter-intuitive circular-polarization dependent second harmonic generation response above 0.2 which is not present in two-dimensional tellurium. Orientation variations in 1D tellurium nanowires obtained by four-dimensional scanning transmission electron microscopy (4D-STEM) and their correlation with unconventional non-linear optical properties by second harmonic generation circular dichroism (SHG-CD) uncovers an unexpected circular-polarization dependent SHG response from 1D nanowire bundles – an order-of-magnitude higher than in single-crystal two-dimensional tellurium structures – suggesting the atomic- and meso-scale crystalline structure of the 1D material possesses an inherent chirality not present in its 2D form; and which is strong enough to manifest even in the aggregate non-linear optical (NLO) properties of aggregates.

Received 5th March 2021,
Accepted 5th May 2021

DOI: 10.1039/d1nr01442k

rsc.li/nanoscale

1. Introduction

Tellurium (Te) is an elemental semiconductor with a high intrinsic crystalline anisotropy. Te is formed by one-dimensional (1D) helixes of covalent bonded Te atoms along the *c*-axis parallel stacked *via* van der Waals forces in a hexagonal array. The atomic chains's inherent helicity yields a natural chirality (or handedness) arising from the broken mirror and inversion symmetry.[1] Te chirality is described by right-handed ($P3_121$ space group no. 152) or left-handed ($P3_221$ space group no. 154) oriented helices. Exciting properties emerge from the crystal anisotropy in 1D and 2D Te, such as anisotropy of the thermal conductivity,[2] photocurrent,[3] and band splitting.[4] The non-centrosymmetric chirality is also responsible for spin texture,[5,6] electrical magneto-chiral,[7] and gyrotropic effects.[8] The chiral lattice of Te also enables activity such as linear and non-linear optical circular dichroism (CD).[9,10] The non-linear CD is much more sensitive to structural asymmetry for nanomaterials than linear CD and can be investigated by the strong dependency of the second-harmonic generation (SHG) on the handedness of the optical excitation.[11]

The preferentially driven growth of Te along the helical chain axis promotes the formation of 1D nanostructures such as nanoribbons, nanotubes, and nanowires (NWs). Ultrathin (sub-10 nm) Te NWs[12–15] exhibit a low density of defects, large carrier mobility and current density, high surface-to-volume ratio, and can exhibit a larger electronic bandgap compared to bulk due to quantum confinement effects which may make them useful in electronic[16] and energy[17,18] applications. Nevertheless, no remarkably anomalous properties have been reported in the literature from the characterization of ultrathin Te NWs.

Inorganic NWs can express chirality beyond the unit cell when a periodic helical twist along their length emerges, and the properties of the nanostructure become orientation dependent. In most cases, this meso-scale helical twist is unrelated to the atomic level chirality of the crystal. Discrete and random twisting in NWs can be described as a rotation of the lattice produced by the following in order of likelihood: (i) spontaneous or controlled formation of topological defects,[19] (ii) modulations in the growth environment,[20] (iii) inherent elastic torque observed only in sub-nanometer NWs,[21,22] or the least likely, (iv) expression of the unit cell anisotropy at the nano/micro-scale.[23] The most common origin of helicity in NWs was first described by Eshelby[24] as a directional twist driven by an axial screw dislocation. The commonly known Eshelby twist relates the Burger's vector and the NW radius to the twist rate.

[a]*Center for Integrated Nanotechnologies, Materials Physics and Applications Division, Los Alamos National Laboratory, Los Alamos, New Mexico 87545, USA. E-mail: pettesmt@lanl.gov*
[b]*Materials Science in Radiation and Dynamics Extremes (MST-8), Materials Science and Technology Division, Los Alamos National Laboratory, Los Alamos, New Mexico 87545, USA*
[c]*NCEM, Molecular Foundry, Lawrence Berkeley National Laboratory, Berkeley, California 94720, USA*
[d]*Department of Materials Science and NanoEngineering, Rice University, Houston, Texas 77005, USA*

†Electronic supplementary information (ESI) available: Additional SHG-CD experimental details. See DOI: 10.1039/d1nr01442k

This formalism has successfully described the helical twist in single (CdSe,[25] Cu,[26] ZnO, InP,[27] GeS,[28–30] AlN[31]) and branched (PbS,[32] PbSe[33]) NWs of sizes in the order of micrometers in length and greater than ~20 nm in diameter. For ultrathin NWs, pure inherent chirality is observed if a periodic twist of origin (iii) or (iv) is formed during the synthesis. So far, chirality has only been detected for occurring natural Te in short-ranges at the atomic level by aberration-corrected scanning transmission electron microscopy;[34] and in synthetically grown Te nanostructures by directing the handedness with additional chiral biomolecules.[35] Due to its high spatial resolution, scanning tunneling microscopy (STM) has been the to-go technique to investigate induced or intrinsic chirality at the molecular level of monolayers created at the solid/liquid interphase;[36–38] and recently extended to ultrathin single walled nanotubes for absolute handedness.[39] Electron diffraction-based technique are conventionally more used for orientation analysis due to their high sensitivity and relative straightforward sample preparation. Electron backscattering diffraction (EBSD) and transmission Kikuchi diffraction (TKD) are excellent examples of techniques used to create orientation maps as they provide inverse pole figures that expand to a large portion of the stereographic sphere. However, orientation analysis of ultrathin Te NWs by conventional high-resolution transmission electron microscopy (TEM) and electron diffraction techniques remains challenging as the NWs scatter weakly and are prone to electron irradiation damage.

In this work, we report the use of four-dimensional scanning transmission electron microscopy (4D-STEM)[40] to identify variations in the crystallographic orientation of Te NWs with sizes of 6 and 17 nm. In 4D-STEM, a set of nanobeam electron diffraction (NBED) patterns is recorded from an array of (x, y) positions in real space. Structural properties can be retrieved from the analysis of the lattice in reciprocal space at each real-space pixel position. The complex dataset was analyzed using open-source and custom-made codes for template matching of individual and representative groups of NBED patterns. Interestingly, a subtle change in the orientation observed by TEM was proven to be a meso-scale helical twist of the NWs. The non-linear optical properties of the chiral ultrathin Te NWs were investigated by SHG-CD, and provide two orders of magnitude larger contrast between left- and right circularly polarized light than linear CD. Our results indicate a previously undetected helical twist in ultrathin Te NWs.

2. Experimental

Materials and methods

All materials were used as received without further purification. Sodium tellurite (Na_2TeO_3, Sigma-Aldrich 400688-10G, 100 mesh, 99%), poly(vinyl pyrrolidone) (PVP, Sigma-Aldrich PVP40-500G, 40 000 g mol^{-1}), hydrazine hydrate solution ($N_2H_4{\cdot}H_2O$, Sigma-Aldrich 18412, 78–82%) and ammonium hydroxide solution (NH_4OH, Sigma-Aldrich 221228-1L-A, 28.0–30.0%) were used as received.

Microwave-enabled synthesis of Te NWs

For the synthesis of tellurium NWs, a general procedure described previously was used.[41] In a representative synthesis, 401 mg of Na_2TeO_3 was placed into a 10 mL glass microwave vial with a micro-stir bar. 137 mg of PVP-40k was added to the vial, followed by 6 mL of distilled water, 171 mL of NH_4OH, and 113 mL of $N_2H_4{\cdot}H_2O$. The mixture was vortexed for about 20 seconds. The glass vial was capped with a specially designed microwave septum. The vial was then placed inside the cavity of a CEM Discovery microwave reactor with a pressure control system attached to the vial. The solution was heated with a heating ramp time of 2–3 minutes to reach 175 °C, with cooling air constantly flowing during the ramping, heating, and cooling stages. The reaction was kept at the desired temperature for 10 minutes while the pressure remained constant. The solution was then cooled under flowing air until the vial temperature reached below 50 °C and/or a gauge pressure of 1–2 lb_f in^{-2} with maximum air flow into the microwave cavity. The resultant solution was transferred to a centrifuge tube with 15–20 mL of absolute ethanol. The obtained reaction mixture was centrifuged for 10 minutes at 7000 rpm.

Electron microscopy and diffraction characterization

A lacey carbon-supported Cu TEM grid with 300 mesh (Ted Pella 01895-F) was prepared by drop-casting ~5 μL of the solution with ultrathin Te NWs and left to dry at ambient conditions. Conventional TEM was obtained on an image-corrected FEI Titan operating at 300 kV with a C2 aperture of 70 μm. Transmission Kikuchi Diffraction (TKD) was conducted in an FEI Apreo SEM operating at 30 kV with a 6.4 nA electron beam current. TEM grid with Te NWs was mounted on a −20° pretilt holder positioned at a working distance of 1.5 mm. Spatially resolved diffraction information was captured on an EDAX Velocity electron backscatter diffraction (EBSD) camera and stored for offline processing. Kikuchi patterns were recorded every 5 nm for the Te NWs and with a 20 nm step for the Te nanoplates. The orientations were indexed to a crystal structure generated within OIM Analysis's structure builder with space group 152, with 4 atoms per unit cell, and with lattice parameters a = 0.44572 nm and c = 0.59290 nm.

4D-STEM acquisition and processing

4D-STEM experiments were performed on a FEI Titan ETEM operating at 300 kV in STEM microprobe mode, with a 10 μm C2 aperture, spot size 10, camera length 160 mm, and a convergence semiangle of 1 mrad. Data collection at each real-space pixel position was performed using a Gatan K3™ IS direct electron detector and a STEMx™ system attached to the microscope. Datasets of thousands of diffraction patterns were recorded with a dwell time of 20 ms per pattern. The data collected was machine- and software-binned to 512 × 512 pixels to increase the signal-to-noise ratio before computational analysis. Data processing and image analysis were performed using the open-source software py4DSTEM[42] and a series of custom-made Python™ and MATLAB® codes.

Non-linear optical spectroscopy

The non-linear circular dichroism was measured by SHG excited at 800 nm with femtosecond pulsed laser (Spectra-Physics Mai Tai). The circularly polarized laser beam was focused onto the sample by an objective lens with NA = 0.45 (Nikon ELWD 20X, ESI Fig. 5a†). The beam was off-centered to create an inclined incidence of about 10°. As a result of reduced effective NA the spot size on the sample was about 3 μm, and the spatial resolution of SHG was about 2 μm, defined as $1/(\sqrt{2})$ of the spot size. The SHG signal was filtered and collected by photon counter (Hamamatsu C11202). The GE124 fused quartz substrates with spin-coated Te samples were piezoelectrically scanned to identify sub-diffraction limited bundles of nanowires in the SHG image (ESI Fig. 5c†). The target sample was then rotated in plane to yield scanning SHG images at different crystalline orientation. ESI Fig. 5b† shows a schematic of the setup for observing non-linear optical CD through SHG.

3. Results and discussion

Ultrathin Te NWs of 5.7 ± 1.1 nm in diameter were synthesized according to our previous report.[41] The synthesis was optimized for NW production, although a small amount of thicker nanoribbons and 2D tellurene was also produced. A typical bright-field (BF) TEM image of a NW bundle is shown in Fig. 1a; the inset shows the selected area electron diffraction (SAED) pattern with indexed rings corresponding to trigonal Te (t-Te). Dark-field (DF) TEM images of the same area were obtained by placing the smaller objective aperture on the {101} and {110} rings as marked in red and blue, respectively, and are presented in Fig. 1b and c. The false-color image in Fig. 1d was constructed by the superposition of the excited reflections in the DF images. Interestingly, along the NWs' growth axis, the contrast attributed to each reflection was not continuous but segmented, suggesting some type of short-range ordering. As described in ref. 41, the synthesis of Te NWs by microwave-enabled chemistry is driven by preferential growth along the helical chain's axis. Previous reports on microwave[43–45] and hydrothermal synthesis[14,46,47] of Te NWs show large crystalline domains with no particular change in orientation and with a low density of intrinsic defects. We note that DF imaging alone cannot preclude an out-of-plane rotation (*e.g.* bending) as the source of the change in the contrast, which can be merely a product of the spatial location and is not necessarily related to any intrinsic rotation of the crystal.

Fig. 1e shows a TEM image of a single NW loaded on a carbon-supported film, which exhibits observable changes in the atomic lattice fringes along the length axis. These orientation changes were most likely not related to bending as the NW lays almost entirely flat on the carbon suspended substrate. Fast-Fourier transforms (FFTs) of different segments along the NW (marked as areas 1–5) show an apparent tilt away from the $[2\bar{1}\bar{1}0]$ zone axis as the higher-order reflections marked in yellow circles shift progressively from left to right. Analysis of several TEM images from NWs with 3–6 nm diameters show similar changes in the FFTs suggesting a possible axial rotation on the NWs axis. For comparison, ESI Fig. 1† presents TEM images of Te nanoplates which do not show any significant change in the orientation as evidenced in the SAED pattern and the FFTs of different areas within a same field of view (FOV). Here we note that the shift of lattice planes in the binned FFTs is not a reliable method to quantify orientation changes or helicity at this scale. Axial rotation can be evidenced in the variation of the diffraction pattern along the NW's length. The weak diffraction of isolated ultrathin NWs and the fast damage to the lattice under e-beam, prevent direct observation of changes in the reciprocal lattice.

Despite the weak diffraction produced by the Te NWs; nano-scaled variations in lattice's orientation can be quantified by using 4D-STEM. In 4D-STEM, crystallographic changes can be identified by comparing the variations in NBED patterns on a 2D array of real space positions. Fig. 2a shows a virtual high-angle annular dark-field (HAADF) STEM image reconstructed from a 98 × 100-pixel array centered around a bundle of larger diameter NWs (16.7 ± 2.0 nm). Individual NBED patterns along two NWs are highlighted, showing changes in intensity and position of disks excited to Bragg's conditions. Tilts of the unit cell with respect to the electron beam axis modify the section of the reciprocal lattice relrods intercepting the Ewald sphere, therefore, changing the diffraction pattern. By analyzing NWs oriented slightly off a major zone axis, the change in NBED patterns became more noticeable as the positions of the lattice vectors were more sensitive to orientation changes.

The average intensity of the 9800 NBED patterns is presented in Fig. 2b and can be visualized as a superposition of a set of NBED patterns from a crystal oriented in different [**uvtw**] zone axes (using Miller-Bravais notation). The virtual annular dark-field (ADF) image formed by selecting the {110} reflections with virtual annular detectors (Fig. 2b, open yellow circles) is presented in Fig. 2c. The real space contrast variation along NW axes in Fig. 2a is segmented with a separation between bright areas of 150–200 nm. Larger diameter NWs and nanoribbons do not always exhibit orientation gradients, in fact, most of the NWs with diameter >10 nm do not show significant changes in the NBED patterns as shown in the 4D-STEM dataset of ESI Fig. 2.†

ESI Fig. 3 and 4† show orientation imaging microscopy (OIM) by means of Transmission Kikuchi Diffraction (TKD) of Te NWs (16.7 ± 2.0 nm) as well as a Te nanoplate (~30 nm thickness), respectively. This technique was chosen as a well-established benchmark to which the 4D-STEM data could potentially be compared against. Kikuchi patterns are formed when the sample is thick enough to produce diffusely scattered electrons (inelastically scattered) to highlight the reciprocal lattice. Ultrathin NWs do not scatter enough diverging electrons to produce a distinctive Kikuchi pattern; therefore, the thicker NWs were analyzed with this technique. In comparison with TKD patterns obtained from Te nanoplates, Te NW pat-

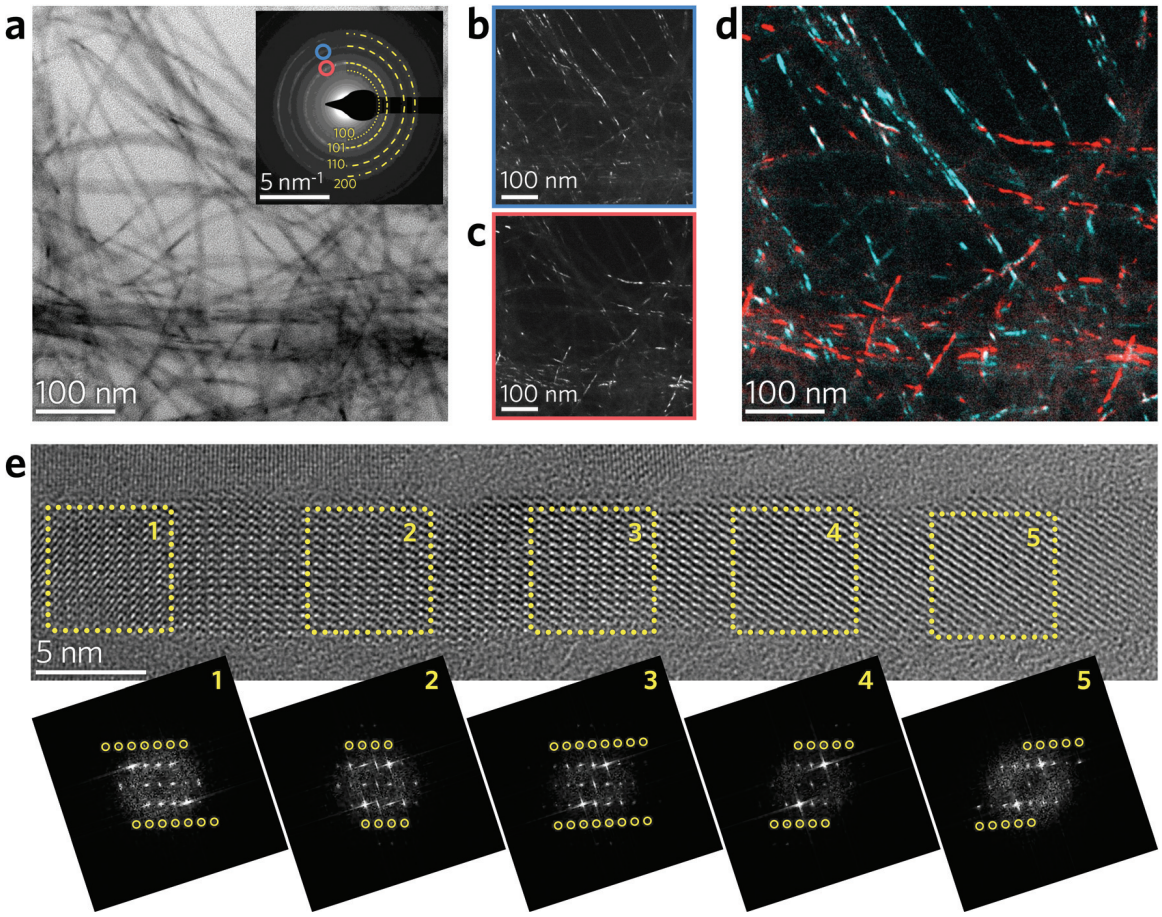

Fig. 1 (a) BF-TEM image of a bundle of Te NWs, inset shows the indexed SAED pattern. (b and c) DF-TEM images constructed by placing the objective aperture near the {101} and {110} reflections denoted by blue and red open circles in (a, inset), respectively. (d) False-color DF-TEM image composited from (b and c). (e) TEM image of a 5.7 nm diameter Te NW and binned FFTs from different areas along the NW's length showing differences in the apparent orientation as evidenced by the change in the higher-order reflections.

terns are significantly fainter with weak orientation signal even after standard post-processing. Close examination showed orientation changes in the thicker nanostructures we were able to characterize with TKD was virtually non-existant as 'changes' corresponded to equivalent and mirror orientations, providing evidence that axial rotation vanishes as the diameter of the NWs increase. The faint signals present in thicker NWs required significant effort to index; thus, 4D-STEM appears to be the most reliable method with which we can directly observe axial rotation in Te NWs. For Te nanoplates the TKD patterns indicate that the single-crystalline nanostructures are uniquely orientated, and no significant variation in the unit cell orientation is detected.

Additional analysis of an 84 nm longitudinal section of an ultrathin Te NW (5.4 nm diameter) lying flat on a carbon membrane was performed to minimize any possible out-of-plane bending. 4D-STEM data sets consisting of NBED patterns were collected from a real space array of 37 × 84-pixels with a 1 nm step size. Using the open-source Python™ repository py4DSTEM,[42] the sub-pixel center position of each diffraction disk in the NBED array was obtained by cross-correlation with a reference probe taken from the vacuum.[48] The collection of 3108 NBED patterns was corrected for both drift and elliptical distortion in reciprocal space. Changes in NW orientation were identified by classifying the NBED patterns into six categorial classes with common diffraction motifs. The initial classifications were obtained by creating subsets of NBED patterns with a co-occurrence of Bragg disks. Refinement of the classes was performed using a non-negative matrix factorization method; additional details about the 4D-STEM data analysis method can be found elsewhere.[42] Real space reconstruction of the diffraction classes is presented in Fig. 3a, where each color represents a particular set or class of NBED patterns.

The discontinuity between classes is not a real segmentation of the NW but is due to the weak detection and classification of NBED patterns near the class edges. Fig. 3b and c shows each class image in real and reciprocal space, respectively. The diffraction class patterns shown in Fig. 3d present each disk's position as a red dot with its weight indicated by the dot's size. The first class (far left, cyan border) has primary lattice vectors indexed as $\mathbf{g_1} = 0\bar{1}0$ and $\mathbf{g_2} = 003$, close to the $\langle 2\bar{1}\bar{1}0 \rangle$ zone axis; as we move rightward along the axis of the

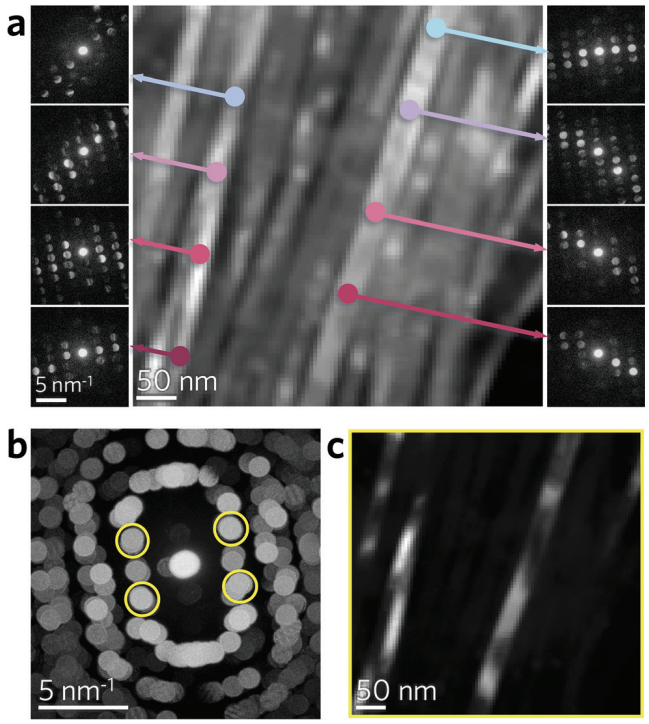

Fig. 2 (a) Virtual HAADF-STEM image from the 4D-STEM dataset. NBED patterns at the marked pixel positions of two NWs show changes in their orientations along their length. (b) Average NBED pattern of the entire array shown in (a), Bragg disk superposition was caused by the contribution of a large set of zone axes. (c) Virtual {110} reflection ADF image constructed from the annular regions marked in yellow open circles in (b).

NW, the class diffraction patterns show a change in the reciprocal lattice relrods in Bragg's condition consistent with a rotation of the unit cell; finally, the last class (far right, green border) primary lattice vectors were indexed as $\mathbf{g_1} = 1\bar{2}0$ and $\mathbf{g_2} = 003$, close to the $\langle 10\bar{1}0 \rangle$ zone axis.

The unit cell rotation along the axis of the NW can be quantified by using a post-imaging custom-made Automated Crystal Orientation Mapping (ACOM) code in MATLAB. Our ACOM algorithm was applied in the postprocessing stage after datasets have been carefully calibrated and corrected for the most common distortions, such as ellipticity. It is important to note that conventional analysis of individual Te NW NBED patterns was complicated since diffraction was often so weak (especially for off-zone-axis regions). For template matching of the NBED patterns, we computed a library with ~33 000 Te diffraction patterns from the atomic positions and lattice vectors of bulk Te (powder diffraction file no. 00-036-1456,[49] space group $P3_121$); covering a 30° high-symmetry range in the stereographic sphere between [0001]–[$2\bar{1}\bar{1}0$]–[$10\bar{1}0$] orientations. The best fit from the library was calculated by defining a score function that initially compared the list of diffraction peaks in the sample with Bragg vector lengths in the diffraction library to create a subset of scoring libraries. The subclass was later compared with the NBED patterns at each pixel position by rotating the library's patterns 360° in 0.1° steps. The score function was calculated for each orientation as the square root of the peak's experimental intensity multiplied by the calculated intensity in the diffraction library.[50] A threshold on the cross-correlation intensity was set to reduce false positives. There was some ambiguity in the orientation analysis due to the 180° symmetry of the crystal and the limited number of

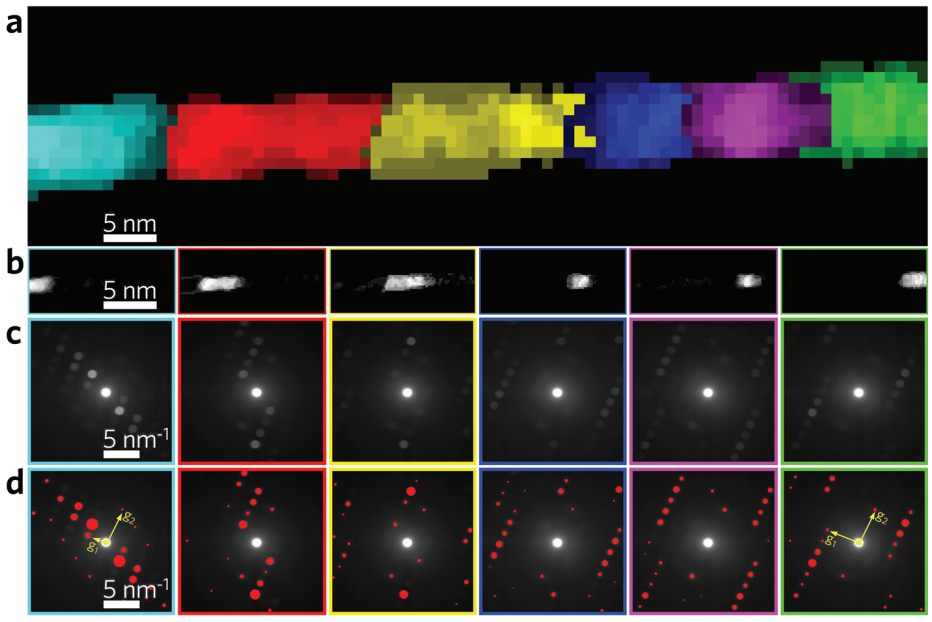

Fig. 3 (a) Reconstructed color-categorized real space image from the 4D-STEM data of an ultrathin Te NW. Each color represents a class of common diffraction patterns. (b) Virtual images were constructed with only the contribution of each class's NBED patterns showing the segmented orientation of the NW. (c) Each class average diffraction pattern, and (d) weighted class patterns. Notice the change in the primary lattice vector $\mathbf{g_1}$ from the first class in cyan color to the last class in green.

Bragg disks excited in a particular experimental configuration (because of the very small diffraction volume); therefore, the proposed solution was not unique. We note that several elements could be introduced in future work to improve the orientation analysis's quality and reliability, producing a more robust and evidently more complex method. Nevertheless, the general conclusion in this work remains true as the presence of an intrinsic meso-scale twist in the Te NWs was evidenced.

Fig. 4a shows a virtual image of the NW and the helical chains's atomic model viewed from the [0001] direction. The ACOM results mapped onto the reduced stereographic triangle viewed from the *z*-direction are also presented. A twist of ~25° within the field of view was identified and the rotation axis was close to the [0001] direction suggesting a helical twist along the NW's axis. This corresponds to a twist rate of approximately 0.2–0.3° nm^{-1}. A diagram showing the most likely path of the helical twist in the projection of the stereographic sphere is shown in Fig. 4b. A limited number of Kikuchi bands and zone axes are shown for reference. The approximate orientation of the categorical classes described in Fig. 3 was obtained by comparing simulated diffraction patterns to track the rotation from the first class (cyan) to the last class (green). The initial class marked with a cyan dot in the stereographic projection was ~7° away of the $[2\bar{1}\bar{1}0]$ zone axis; as we move along the length of the NW, the classes move nearly parallel to the 003 Kikuchi band towards the $[10\bar{1}0]$ zone axis. The final class (green) lies around 4° away from the $[10\bar{1}0]$.

The misorientation angle between the best-fit [**uvtw**] direction and the $[2\bar{1}\bar{1}0]$ zone axis for each of the NBED patterns along the NW's length is shown in Fig. 4c. The individual fit of the weakly scattering NBED patterns was imprecise, as evidenced by the discontinuity and large jumps in misorientation angle in orientations where few Bragg disks were excited. One-dimensional experimental patterns and patterns with a non-uniform contribution in the intensity distribution will not be correctly 'matched' with the template. As a result, the 'best-fit' on a subset of NBED patterns will not necessarily be the right match. For example, a set of patterns wrongly overestimate the misorientation angle to 35–38°; another set, between 25 to 35 nm in the *z* length of the NW, have an inaccurate and ambiguous best-fit match to a direction at ~7° or ~25° without anything in between. On the other hand, analysis of the six diffraction classes shows a smooth increase in the angle from ~6° to ~27° in relatively uniform *z* increments. This is the advantage of our class-based algorithm in specific cases such as weak scattering nanomaterials, where classification can actually lead to better correlation due to the increase signal-to-noise ratio of the average class compared to the individual NBED patterns. The calculated twist rate shows the minimum length of the NW necessary to detect a change in the zone axis (every 30°) was about ~100–150 nm, very similar (although much more accurate) to what the virtual HAADF of Fig. 2c infers. Historically, the subtle helicity of ultrathin Te NWs has been elusive. We speculate that the limited FOV for high

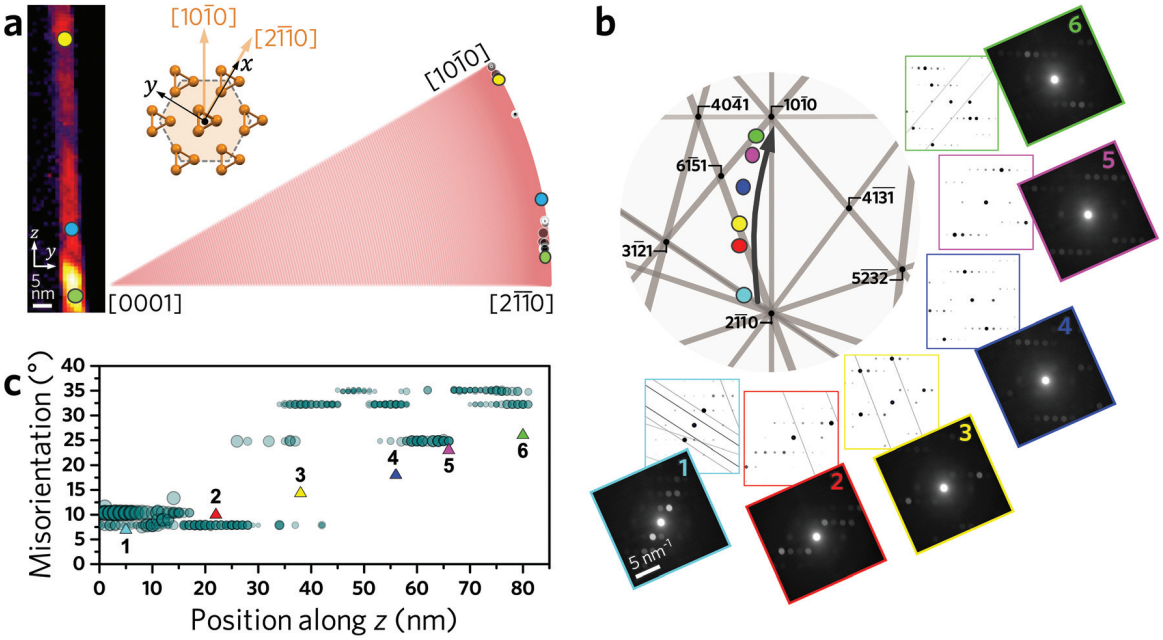

Fig. 4 (a) Virtual image of the Te NW, atomic model of the Te unit cell viewed along the *c*-axis (*z*-direction), and reduced stereographic triangle showing the best-fit orientation map of all the NBED patterns within the Te NW. Filled circles serve as a visual guide between reciprocal and real space. (b) Using the approximate match of simulated patterns with the six diffraction classes (identical color code used in Fig. 3), the path of the change in orientation along the NW length is shown on a section of the stereographic sphere's projection. The rotation axis of the unit cell is nearly parallel to the [0001] direction. (c) Misorientation angle from the $[2\bar{1}\bar{1}0]$ zone axis, green circles represent all the pixels along the length of the NW, sized by score. The average misorientation angle for the six diffraction classes is shown for comparison. An orientation change of ~25° along the 84 nm length analyzed here is evidence of meso-scale helical twist in the ultrathin NW.

resolution TEM and long-range bending of large FOV suspended samples used in diffraction-based analyses have been responsible for the unnoticed periodic twist in prior reports.

SHG-CD confirmed chirality in the intrinsic helical twist of the ultrathin Te NWs, as the SHG intensity varies when excited with left-handed circularly polarized (LCP) and right-handed circularly polarized (RCP) light. To accurately determine the NWs' location, the samples were mounted on a piezoelectric scanning stage. The circularly polarized 800 nm pulse incidents at an angle θ with respect to the normal vector of the sample plane as shown in ESI Fig. 5† along with scanning SHG images of the 1D NWs and 2D plate samples investigated here. The total SHG-CD signal without discriminating the polarization was collected in the direction of specular reflection. Fig. 5a shows the SHG intensity from left- and right-circularly polarized light as a function of the angle ϕ between a representative NW bundle's axial direction and the incident plane of light. Fig. 5b shows SHG intensities for a representative two-dimensional (2D) nanoplate.

The SHG-CD (Fig. 5c) is then defined from the LCP and RCP SHG intensities, I_{LCP} and I_{RCP} respectively, as

$$\text{SHG-CD} \equiv \frac{|I_{LCP} - I_{RCP}|}{(I_{LCP} + I_{RCP})/2} \quad (1)$$

and was up to 0.23 at certain incident angles, which is two orders of magnitude larger than what would be expected from linear CD.[10] The asymmetry of the angular pattern and the degree of SHG-CD were determined by both the morphological twisting and the crystalline orientation, and therefore varied at different locations or between samples, but were generally prominent for NW bundles.[11] By contrast, as-grown 2D Te nanoplates do not exhibit significant SHG-CD above the uncertainty level of ~0.05, as shown in Fig. 5d. This lack of SHG-CD signal in 2D Te indicates minimal chirality contribution from either morphology or atomic lattices (ESI Fig. 5†).[51]

The SHG-CD results corroborate the net chirality enabled by nanoscale helical twist of the Te NWs found with 4D-STEM characterization. TEM images of ~70 nm segments of NWs show no evidence of axial screw dislocations in the lattice fringes; which is the common source of Eshelby twist in previously reported NWs of 30 nm,[27] 50 nm,[25,26] and 100 nm (ref. 52) in diameter. We hypothesize that the intrinsic helical nature of ultrathin Te NWs is a product of residual stress in the anisotropic crystalline structure due to the NWs' large aspect ratio, causing a warping displacement of the lattice along the *c*-axis that follows the chirality of the atomic helical chain. Similar results have been proposed for NWs with diameter bellow 10 nm,[53] and experimentally observed on $CaCO_3$ NWs grown in confinement.[23] To further confirm the net chirality of the Te NWs (and other 1D NWs) it is necessary to correlate the direction and modulation of the lattice fringes with

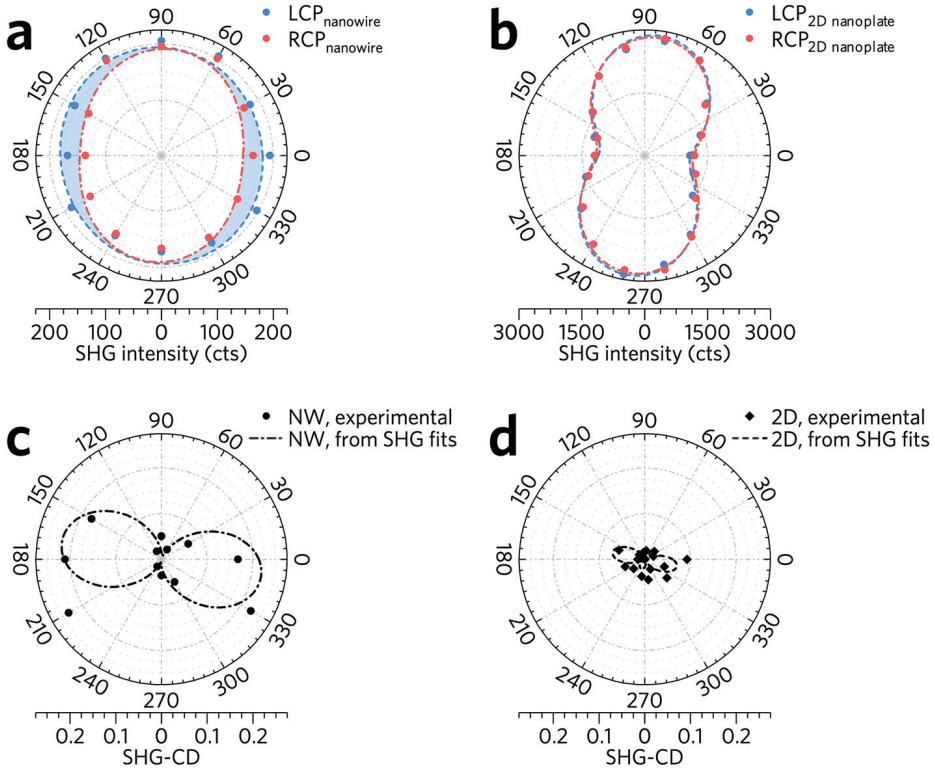

Fig. 5 (a) SHG intensity from a Te NW bundle excited with left- and right-hand circularly polarized light as a function of crystalline orientation, defined as the angle between the axis of the NW bundle and the normal vector of the plane in which light propagates. (b) SHG signal from a 2D Te nanoplate. (c) SHG-CD of a Te NW bundle obtained from (a) per eqn (1). (d) SHG-CD of a 2D nanoplate was on the order of the uncertainty level (~0.05).

the unit cell by using complementary techniques such as STM. It is possible that meso-scale helicity is a property belonging to all 1D NW forms of materials with chiral atomic structures. Such an attractive field of research remains open and is out of the scope of this work.

4. Conclusion

In summary, we have identified an intrinsic helical twist in ultrathin Te NWs. This elusive twist was reported by means of 4D-STEM acquisition of thousands of NBED patterns. Orientation variations along the NW axis were quantified using classification and a template matching custom-made ACOM script. For weak scattering and electron irradiation sensitive materials such as ultrathin Te NWs, orientation changes were more reliably detected in a set of common diffraction classes over individual NBED patterns. Evidence of a ~25° rotation about the [0001] axis was observed over an 84 nm length segment. Although the path of the rotation has no unique solution in reciprocal space, the rotational symmetry of the crystal allows us to calculate a twist rate of 0.2–0.3° nm^{-1}. SHG-CD confirms net chirality in the NWs that persists even for bundles, in contrast to the nanoplates. This may indicate a signature of non-symmorphic topology in an air-stable material with controllable structure during growth.

Conflicts of interest

There are no conflicts to declare.

Acknowledgements

This work was supported by the Laboratory Directed Research and Development program of Los Alamos National Laboratory under project numbers 20190516ECR and 20210036DR (M. T. P., A. L.-C.), and the National Security Education Center under project numbers IMS RR19PETT and IMS RR21PETT (M. T. P., A. L.-C.), and was performed at the Center for Integrated Nanotechnologies, an Office of Science User Facility operated for the U.S. Department of Energy (DOE) Office of Science. Los Alamos National Laboratory, an affirmative action equal opportunity employer, is managed by Triad National Security, LLC for the U.S. Department of Energy's NNSA, under contract 89233218CNA000001. Work at the Molecular Foundry was supported by the Office of Science, Office of Basic Energy Sciences, of the U.S. Department of Energy under Contract no. DE-AC02-05CH11231. B. H. S. and the development of py4DSTEM was supported by the Toyota Research Institute. C. O. acknowledges additional support from the Department of Energy Early Career Research Award program. Non-linear optical spectroscopy at Rice university was supported by the U.S. National Science Foundation (NSF) under award number DMR 2005096.

References

1 Z. He, Y. Yang, J.-W. Liu and S.-H. Yu, *Chem. Soc. Rev.*, 2017, **46**, 2732–2753.
2 S. Huang, M. Segovia, X. Yang, Y. R. Koh, Y. Wang, P. D. Ye, W. Wu, A. Shakouri, X. Ruan and X. Xu, *2D Mater.*, 2019, **7**, 015008.
3 G. Siyan, S. Changqing and Z. Xi, *Nanophotonics*, 2019, **9**, 1931–1940.
4 G. Jnawali, Y. Xiang, S. M. Linser, I. A. Shojaei, R. Wang, G. Qiu, C. Lian, B. M. Wong, W. Wu, P. D. Ye, Y. Leng, H. E. Jackson and L. M. Smith, *Nat. Commun.*, 2020, **11**, 3991.
5 M. Sakano, M. Hirayama, T. Takahashi, S. Akebi, M. Nakayama, K. Kuroda, K. Taguchi, T. Yoshikawa, K. Miyamoto, T. Okuda, K. Ono, H. Kumigashira, T. Ideue, Y. Iwasa, N. Mitsuishi, K. Ishizaka, S. Shin, T. Miyake, S. Murakami, T. Sasagawa and T. Kondo, *Phys. Rev. Lett.*, 2020, **124**, 136404.
6 M. Hirayama, R. Okugawa, S. Ishibashi, S. Murakami and T. Miyake, *Phys. Rev. Lett.*, 2015, **114**, 206401.
7 G. L. J. A. Rikken and N. Avarvari, *Phys. Rev. B*, 2019, **99**, 245153.
8 S. S. Tsirkin, P. A. Puente and I. Souza, *Phys. Rev. B*, 2018, **97**, 035158.
9 M. Cheng, S. Wu, Z.-Z. Zhu and G.-Y. Guo, *Phys. Rev. B*, 2019, **100**, 035202.
10 H. Stolze, M. Lutz and P. Grosse, *Phys. Status Solidi B*, 1977, **82**, 457–466.
11 J. D. Byers, H. I. Yee, T. Petralli-Mallow and J. M. Hicks, *Phys. Rev. B: Condens. Matter Mater. Phys.*, 1994, **49**, 14643–14647.
12 T. I. Lee, S. Lee, E. Lee, S. Sohn, Y. Lee, S. Lee, G. Moon, D. Kim, Y. S. Kim, J. M. Myoung and Z. L. Wang, *Adv. Mater.*, 2013, **25**, 2920–2925.
13 G. Xi, Y. Liu, X. Wang, X. Liu, Y. Peng and Y. Qian, *Cryst. Growth Des.*, 2006, **6**, 2567–2570.
14 J.-W. Liu, J.-H. Zhu, C.-L. Zhang, H.-W. Liang and S.-H. Yu, *J. Am. Chem. Soc.*, 2010, **132**, 8945–8952.
15 J.-K. Qin, P.-Y. Liao, M. Si, S. Gao, G. Qiu, J. Jian, Q. Wang, S.-Q. Zhang, S. Huang, A. Charnas, Y. Wang, M. J. Kim, W. Wu, X. Xu, H.-Y. Wang, L. Yang, Y. Khin Yap and P. D. Ye, *Nat. Electron.*, 2020, **3**, 141–147.
16 A. Kramer, M. L. Van de Put, C. L. Hinkle and W. G. Vandenberghe, *npj 2D Mater. Appl.*, 2020, **4**, 10.
17 S. Yazdani and M. T. Pettes, *Nanotechnology*, 2018, **29**, 432001.
18 A. Sahu, B. Russ, M. Liu, F. Yang, E. W. Zaia, M. P. Gordon, J. D. Forster, Y.-Q. Zhang, M. C. Scott, K. A. Persson, N. E. Coates, R. A. Segalman and J. J. Urban, *Nat. Commun.*, 2020, **11**, 2069.
19 B. Sung, A. de la Cotte and E. Grelet, *Nat. Commun.*, 2018, **9**, 1405.
20 S. Ibaraki, R. Ise, K. Ishimori, Y. Oaki, G. Sazaki, E. Yokoyama, K. Tsukamoto and H. Imai, *Chem. Commun.*, 2015, **51**, 8516–8519.

21 A. L. Koh, S. Wang, C. Ataca, J. C. Grossman, R. Sinclair and J. H. Warner, *Nano Lett.*, 2016, **16**, 1210–1217.
22 J. Lin, Y. Zhang, W. Zhou and S. T. Pantelides, *ACS Nano*, 2016, **10**, 2782–2790.
23 A. Verch, A. S. Côté, R. Darkins, Y. Y. Kim, R. V. D. Locht, F. C. Meldrum, D. M. Duffy and R. Kröger, *Small*, 2014, **10**, 2697–2702.
24 J. D. Eshelby, *J. Appl. Phys.*, 1953, **24**, 176–179.
25 H. Wu, F. Meng, L. Li, S. Jin and G. Zheng, *ACS Nano*, 2012, **6**, 4461–4468.
26 F. Meng and S. Jin, *Nano Lett.*, 2012, **12**, 234–239.
27 D. Ugarte, L. H. G. Tizei, M. A. Cotta, C. Ducati, P. A. Midgley and A. S. Eggeman, *Nano Res.*, 2019, **12**, 939–946.
28 P. Sutter, S. Wimer and E. Sutter, *Nature*, 2019, **570**, 354–357.
29 P. Sutter, J.-C. Idrobo and E. Sutter, *Adv. Funct. Mater.*, 2020, **31**, 2006412.
30 Y. Liu, J. Wang, S. Kim, H. Sun, F. Yang, Z. Fang, N. Tamura, R. Zhang, X. Song, J. Wen, B. Z. Xu, M. Wang, S. Lin, Q. Yu, K. B. Tom, Y. Deng, J. Turner, E. Chan, D. Jin, R. O. Ritchie, A. M. Minor, D. C. Chrzan, M. C. Scott and J. Yao, *Nature*, 2019, **570**, 358–362.
31 F. Meng, M. Estruga, A. Forticaux, S. A. Morin, Q. Wu, Z. Hu and S. Jin, *ACS Nano*, 2013, **7**, 11369–11378.
32 M. J. Bierman, Y. K. A. Lau, A. V. Kvit, A. L. Schmitt and S. Jin, *Science*, 2008, **320**, 1060–1063.
33 J. Zhu, H. Peng, A. F. Marshall, D. M. Barnett, W. D. Nix and Y. Cui, *Nat. Nanotechnol.*, 2008, **3**, 477–481.
34 Z. Dong and Y. Ma, *Nat. Commun.*, 2020, **11**, 1588.
35 A. Ben-Moshe, S. G. Wolf, M. B. Sadan, L. Houben, Z. Fan, A. O. Govorov and G. Markovich, *Nat. Commun.*, 2014, **5**, 4302.
36 K.-H. Ernst, *Phys. Status Solidi B*, 2012, **249**, 2057–2088.
37 G. P. Lopinski, D. J. Moffatt, D. D. M. Wayner and R. A. Wolkow, *Nature*, 1998, **392**, 909–911.
38 J. A. A. W. Elemans, I. De Cat, H. Xu and S. De Feyter, *Chem. Soc. Rev.*, 2009, **38**, 722–736.
39 A. I. A. Abd El-Mageed and T. Ogawa, *Chirality*, 2020, **32**, 345–352.
40 C. Ophus, *Microsc. Microanal.*, 2019, **25**, 563–582.
41 A. Londoño-Calderon, D. J. Williams, C. Ophus and M. T. Pettes, *Small*, 2020, **16**, 2005447.
42 B. H. Savitzky, L. A. Hughes, S. E. Zeltmann, H. G. Brown, S. Zhao, P. M. Pelz, E. S. Barnard, J. Donohue, L. R. DaCosta and T. C. Pekin, *arXiv*, 2020, arXiv:2003.09523, https://arxiv.org/abs/2003.09523.
43 Y.-J. Zhu and X.-L. Hu, *Chem. Lett.*, 2003, **32**, 732–733.
44 Y. J. Zhu, W. W. Wang, R. J. Qi and X. L. Hu, *Angew. Chem., Int. Ed.*, 2004, **43**, 1410–1414.
45 J.-W. Liu, F. Chen, M. Zhang, H. Qi, C.-L. Zhang and S.-H. Yu, *Langmuir*, 2010, **26**, 11372–11377.
46 K. Wang, Y. Yang, H.-W. Liang, J.-W. Liu and S.-H. Yu, *Mater. Horiz.*, 2014, **1**, 338–343.
47 H.-S. Qian, S.-H. Yu, J.-Y. Gong, L.-B. Luo and L.-F. Fei, *Langmuir*, 2006, **22**, 3830–3835.
48 T. C. Pekin, C. Gammer, J. Ciston, A. M. Minor and C. Ophus, *Ultramicroscopy*, 2017, **176**, 170–176.
49 T. P. Smorodina, *Sov. Phys. Solid State*, 1960, **2**, 807–809.
50 X. Hong, S. E. Zeltmann, B. H. Savitzky, L. R. DaCosta, A. Müller, A. M. Minor, K. C. Bustillo and C. Ophus, *Microsc. Microanal.*, 2020, **27**, 129–139.
51 A. Londoño-Calderon, D. J. Williams, M. M. Schneider, B. H. Savitzky, C. Ophus and M. T. Pettes, *J. Phys. Chem. C*, 2021, **125**, 3396–3405.
52 S. A. Morin and S. Jin, *Nano Lett.*, 2010, **10**, 3459–3463.
53 M. Gailhanou and J.-M. Roussel, *J. Appl. Crystallogr.*, 2018, **51**, 1586–1596.